Ensemble Optimal Interpolation: multivariate properties in the Gulf of Mexico

By FRANÇOIS COUNILLON* and LAURENT BERTINO, *Mohn Sverdrup Center/Nansen Environmental and Remote Sensing Center, Thormøhlensgate 47, Bergen, Norway*

ABSTRACT

High-resolution models can reproduce mesoscale dynamics and the variability in the Gulf of Mexico (GOM), but cannot provide accurate locations of currents without data assimilation (DA). We use the computationally cheap Ensemble Optimal Interpolation (EnOI) in conjunction with the Hybrid Coordinate Ocean Model (HYCOM) model for assimilating altimetry data. The covariance matrix extracted from a historical ensemble, is three-dimensional and multivariate. This study shows that the multivariate correlations with sea level anomaly are coherent with the known dynamics of the area at two locations: the central part of the GOM and the upper slope of the northern shelf. The correlations in the first location are suitable for an eddy forecasting system, but the correlations in the second location show some limitations due to seasonal variability. The multivariate relationships between variables are reasonably linear, as assumed by the EnOI. Our DA set-up produces little noise that is dampened within 2 d, when the model is pulled strongly towards observations. Part of it is caused by density perturbations in the isopycnal layers, or artificial caballing. The DA system is demonstrated for a realistic case of Loop Current eddy shedding, namely Eddy Yankee.

1. Introduction

The dynamics in the Gulf of Mexico (GOM) are dominated by the powerful northward Yucatan Current flowing into the semi-enclosed basin composed of the resident Gulf Common Water (GCW). The Yucatan Current Water (YCW) originates from tropical regions, and is warmer and more saline than the GCW. This current forms a loop (called the Loop Current, LC) and exits through the Florida Straits, becoming the Gulf Stream. At irregular intervals (Vukovich, 1988; Sturges and Leben, 2000) the LC sheds large eddies that propagate westwards across the GOM. These eddies can be problematic for the offshore industry operating in the northern shelf of the GOM because large velocities are located at their fronts, and accurate forecasts of their fronts are needed.

Many models are able to reproduce the dynamics of the area and its variability (Oey et al., 2005b), but they cannot provide accurate forecasts of mesoscale current features without observations. Indeed, the eddy shedding involves a rapid growth of non-linear instabilities (Cherubin et al., 2005b), and these are difficult to forecast (Chassignet et al., 2005; Kantha et al., 2005b; Oey et al., 2005a). A procedure called data assimilation (DA) computes the most likely model state given a dynamical model

and a set of measurements. Altimetry data provide a good representation of the mesoscale variability in the GOM away from the coast and can be used for DA.

In the case of low dimensional linear dynamical systems, the DA problem is solved by standard techniques like the Kalman Filter (Kalman, 1960), or the adjoint methods. However, in real geophysical applications the system is non-linear and the assumptions of non-biased and Gaussian variables do not apply. Advanced DA methods, like the Ensemble Kalman Filter and Smoother (EnKF/EnKS; Evensen, 2006) and four-dimensional-variational methods (Bennett, 2002) are successful with nonlinear systems using computational costs of about 100 times those of the forward model. It is worth noting that these advanced DA methods rely on unbiased and multivariate Gaussian error statistics.

In the GOM, high-resolution models are needed to resolve the mesoscale dynamics, and computer intensive DA methods are still out of reach. Among the sequential Optimal Interpolation (OI) DA methods, the one developed by Cooper and Haines (1996) is widely used (Chassignet et al., 2005).

Cooper and Haines (1996) use a translation-invariant covariance, based on the geostrophic balance. It applies a vertical rearrangement of water parcels without modifying their temperature, salinity and potential vorticity. The method conserves the water masses and maintains geostrophy in simple cases, for example, far from continental shelves or from regions of strong baroclinic flow.

*Corresponding author.
e-mail: francois.counillon@nersc.no

In the GOM, the fronts of the LC and associated eddies have a clear signal in the sea surface height (SSH). These fronts generally distinguish the YCW from the GCW. Thus, DA should modify temperature and salinity accordingly with SSH within each isopycnal layer. For this purpose, the Multivariate Optimum Interpolation (MVOI; Cummings, 2005) applies Cooper and Haines (1996) method and corrects the vertical temperature and salinity in the water column using the modular ocean data assimilative system (MODAS; Fox et al., 2002). The MODAS computes temperature at depth from sea level anomaly (SLA) using stored regressions of climate anomalies of temperature and dynamic height. Salinity is then computed from the synthetic temperature. The quality of the vertical projection depends on the sampling of the observations used in the climatology. We prefer a relationship that depends on the quality of the dynamical model.

Hence, an OI scheme devised from the EnKF computes the analysis in the space spanned by a stationary ensemble of sampled model state (e.g. during a long model integration). This approach is called the Ensemble OI (EnOI; Oke et al., 2002; Evensen, 2003). The EnOI assumes that temporal variability is representative of the forecast error. This assumption is strong and is surely not always satisfied, but one can expect the updates to be statistically valid over a large number of updates. In the GOM, it is likely that both the temporal variability and the forecast error are dominated by the position of the LC and associated eddies, and therefore the EnOI should be suited. Oke et al. (2005) have demonstrated the EnOI for an eddy-resolving problem of the Australian region.

Other methods obtain their error covariance from a historical ensemble, such as the fixed-basis singular evolutive extended Kalman Filter (SEEK; Brasseur and Verron, 2006). The main differences with the EnOI are the reduction of the ensemble by empirical orthogonal functions (EOFs), and a post-processing step inspired by Cooper and Haines (1996).

Oey et al. (2005a) have tested the forecasting capability of a method similar to the EnOI in the GOM. However, it is interesting to analyse the multivariate properties of the EnOI considering known processes of the area, and to assess the veracity of the multi-Gaussian hypothesis, which is assumed in the EnOI. We use statistical analysis tools (e.g. scatterplots, wavelet analysis) that are not widespread in the oceanographic DA community. Those are also applicable to other ensemble-based DA methods.

The outline of this paper is as follows. The DA system is presented in Section 2. It outlines the theory of the EnOI in Section 2.1, followed by a description of the measurement system in Section 2.2, and of the dynamical model in Section 2.3. The multivariate error statistics computed from the historical ensemble are presented in Section 3, for two characteristic locations in the GOM. A localization technique that removes the spurious long-range correlation, is presented in Section 3.3. The EnOI is tested during the shedding of Eddy Yankee, with a focus on the multivariate consistency of the update (in Section 4.1), on the accuracy of the forecast (in Section 4.2) and on the conservation of the model balance (in Section 4.3). Discussions and conclusions are given in Section 5.

2. Data assimilative system

A DA system finds the best model estimate, given a dynamical model and measurements. Its accuracy depends on the skill of the forward model, the number and the quality of the measurements, and on the methodology that combines the two sources of information considering their respective error statistics.

2.1. The ensemble optimal interpolation

The DA problem consists of accommodating the model equations with measurements. As a deterministic problem, it is overdetermined and generally has no solution. Indeed, neither the model forecast nor the measurements are fully correct, and stochastic errors for the forecast (ϵ) and the measurements (Υ) are introduced into the system as

$$\mathbf{d} = \mathbf{H}\boldsymbol{\psi}^{\mathrm{t}} + \boldsymbol{\Upsilon} \tag{1}$$

and

$$\boldsymbol{\psi}^{\mathrm{f}} = \boldsymbol{\psi}^{\mathrm{t}} + \boldsymbol{\epsilon}, \tag{2}$$

where $\mathbf{d}$ depicts the measurements, $\boldsymbol{\psi}^{\mathrm{f}}$ the model forecast, $\boldsymbol{\psi}^{\mathrm{t}}$ the true state and $\mathbf{H}$ the measurement operator relating the prognostic model state to the measurements.

The problem then becomes underdetermined and has infinitely many solutions. It is assumed that the distributions of the measurement errors (Υ) and the forecast error (ϵ) are Gaussian and non-biased. The precise condition is a multi-Gaussian hypothesis, which requires a Gaussian distribution for each variable, and a linear relationship between all variables (Bertino et al., 2003). Under these assumptions, it becomes possible to calculate a least-square estimate $\boldsymbol{\psi}^{\mathrm{a}}$, which minimizes the distance to $\boldsymbol{\psi}^{\mathrm{t}}$.

In the EnKF, the model covariance matrix is computed at each assimilation step using a Monte Carlo method, whereas in the EnOI, it is stationary and calculated from a historical ensemble as

$$\overline{\boldsymbol{\epsilon}\boldsymbol{\epsilon}^{\mathrm{T}}} \approx \frac{\alpha}{N-1}\mathbf{A}'\mathbf{A}'^{\mathrm{T}}, \tag{3}$$

where $\mathbf{A}'$ is the centered historical ensemble (i.e. $\mathbf{A}' = \mathbf{A} - \overline{\mathbf{A}}$), and $\mathbf{A}$ is the historical ensemble composed of model states. Here, the overbar denotes ensemble averaging or expected value. N is the ensemble size. However, an ensemble of model states sampled over a long time period may have a large seasonal, or interannual variance, which is inadequate to represent the instantaneous forecast error variance, therefore a scaling factor α ($\in (0, 1]$) is introduced.

Similarly, we sample the measurement error covariance matrix as

$$\overline{\boldsymbol{\Upsilon}\boldsymbol{\Upsilon}^{\mathrm{T}}} \approx \frac{1}{N-1}\mathbf{T}\mathbf{T}^{\mathrm{T}}. \qquad (4)$$

To obtain realistic correlations, two conditions are necessary:

(1) The variability of the ensemble of state should be representative of the instantaneous forecast error ϵ.

(2) The multivariate relationships should be linear.

These particular points will be analysed in the following Section 3. The classical Kalman Filter equation is solved as

$$\boldsymbol{\psi}^{\mathrm{a}} = \boldsymbol{\psi}^{\mathrm{f}} + \alpha\mathbf{A}'\mathbf{A}'^{\mathrm{T}}\mathbf{H}^{\mathrm{T}}\left(\alpha\mathbf{H}\mathbf{A}'\mathbf{A}'^{\mathrm{T}}\mathbf{H}^{\mathrm{T}} + \mathbf{T}\mathbf{T}^{\mathrm{T}}\right)^{-1}\left(\mathbf{d} - \mathbf{H}\boldsymbol{\psi}^{\mathrm{f}}\right). \quad (5)$$

The analysis equations can be rearranged as

$$\boldsymbol{\psi}^{\mathrm{a}} = \boldsymbol{\psi}^{\mathrm{f}} + \alpha\mathbf{A}'\boldsymbol{x}, \qquad \text{with} \qquad \boldsymbol{x} \in \mathcal{R}^{\mathrm{N}}, \qquad (6)$$

meaning that $\boldsymbol{\psi}^{\mathrm{a}}$ is a combination of centered model states from the ensemble added to the forecast $\boldsymbol{\psi}^{\mathrm{f}}$. It implies that the updates are three-dimensional and multivariate. The dynamical balance of the model is preserved as long as the model is linear, and thus relies on weak non-linearity of the model. Note that increasing α is equivalent to reducing the observation error.

2.2. Measurements

Near real-time altimetry observations of the ocean are achieved by combining data from numerous satellites. The altimetry data in the GOM provide a useful indication of the main circulation and are suitable for DA (Chassignet et al., 2005; Oey et al., 2005a). Altimetry data show clearly the LC and associated anticyclonic eddies, smaller cyclonic eddies and small vortices that are found closer to the shelf area.

The SLA data used for assimilation are the maps provided by Ssalto/Duacs on a $1/3°$ Mercator grid (Le Traon et al., 2003). Maps are processed from the full cycle of multiple altimeter missions (Jason–1, Envisat, GFO), and are available in near real-time, delayed by one week. They are obtained by time and space interpolation of the along tracks, which include data that are 3 d posterior to the date of the map, and tides are removed using a tidal model, see Ducet et al. (2000).

However, altimetry data are inaccurate close to the coast on the one hand because they are polluted by land measurements, and on the other hand because of imperfections in the tidal model used. We have thus selected measurements only in water deeper than 300 m, which corresponds in the GOM to area 50 km away from the coast.

The measurement error distribution for altimetry can be considered as Gaussian. The standard deviation of the measurements is assumed to be constant, and we use the average value specified by the provider in the GOM area (3 cm). The maps are interpolated in space, and therefore the measurement errors are spatially correlated. The space and time inhomogeneity of
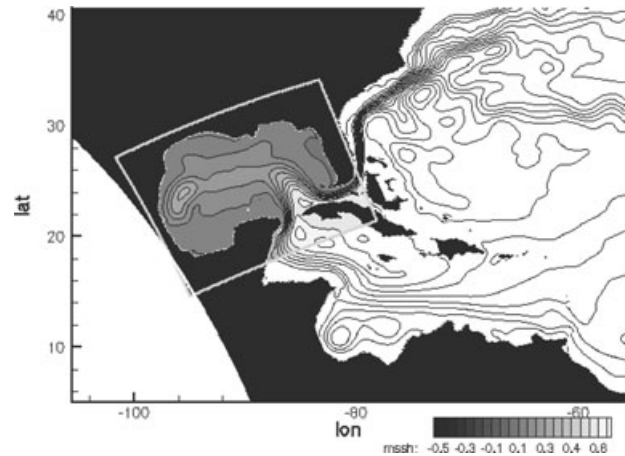

Fig. 1. Mean SSH of TOPAZ3 interpolated into the high-resolution local model grid delimited by the grey box.

the tracks data makes the real mapping error covariance spatially non-stationary, and thus impossible to model with simple two-dimensional function. We use a Gaussian covariance with a decorrelation radius of 50 km, which gives a rough estimate.

2.3. The nested model system

The skill of the forward model is very important in a DA system because it controls the model drift from the initial state, and even more so in the EnOI since the correlations depend on the model ability to reproduce the dynamics. Chassignet et al. (2005) demonstrate the skill of the Hybrid Coordinate Ocean Model (HYCOM) for the GOM, emphasizing the importance of horizontal resolution. Furthermore Oey et al. (2003) and Abascal et al. (2003) show that the inflow through the Yucatan Straits is important with respect to the timing of eddy shedding events. A nested configuration can satisfy these two requirements with reasonable computing cost. The TOPAZ3 system provides six-hourly lateral boundary conditions to a high-resolution model of the GOM (see Fig. 1), using lateral boundary techniques described in Browning and Kreiss (1982). For the slow varying variables, for example, baroclinic velocities, temperature, salinity and layer interface, a simple relaxation technique is used. For the barotropic components (velocities and pressure), the boundary conditions are computed exactly while taking into consideration both the waves propagating into the regional model from the external solution and the waves propagating out through the boundary from the regional model. This constitutes the standard nesting procedure with HYCOM, with an additional horizontal interpolation to the nested model grid. Note that tides are not included, because they are small in the GOM.

The TOPAZ is a real-time forecasting system established for the Atlantic and Arctic basins using HYCOM. It is capable of monitoring the circulation patterns in the Atlantic (Chapter 15 in Evensen, 2006; http://topaz.nersc.no/). The grid is created

using a conformal mapping of the poles to two new locations by the algorithm outlined in Bentsen et al. (1999). The TOPAZ3 horizontal resolution varies from 11 km in the Artic to 18 km near the Equator (approximately 1/8°). The model is initialized from the GDEM3 climatology (Teague et al., 1990) and spin-up for 16 yr. The TOPAZ3 system transports 19.5 Sv into the GOM, instead of the 23.8 Sv measured in CANEK programme during the same 10-month period (Sheinbaum et al., 2002). Note that TOPAZ3 9-yr average net transport is usually of 22 Sv. The structure of the inflow agrees well with the measurements, with the exception that the subtropical underwater (SUW) is too fresh (36.45 instead of 36.6 psu). The TOPAZ3 used in this work does not include DA.

Our high-resolution model is set-up with a 5 km horizontal resolution, which is sufficiently high to resolve the mesoscale features considering the first-mode (baroclinic) Rossby radius ($R_o \simeq 30$ km in the area; Oey et al., 2005b). The model is using a fourth-order numerical schemes for treating the advection of momentum in the primitive equations (Winther et al., 2006). To minimize the necessary spin-up time, the initial state is interpolated from an equilibrium state of TOPAZ3, and spun up for 3 yr.

In HYCOM, the vertical coordinate is isopycnal in the open, stratified ocean, but smoothly reverts to a z-level coordinate in the mixed layer and/or unstratified seas (Bleck, 2002). Both models use 22 hybrid layers, with the minimum thickness of the top layer of 3 m.

The bathymetry is specified using the General Bathymetric Chart of the Oceans database (GEBCO) with $1'$ resolution, interpolated to the model grids. The two models are forced by the six-hourly and 0.5° analysed fields from the European Center for Medium range Weather Forecasting (ECMWF). The models use monthly average river discharge value taken from Dai and Trenberth (2002) and Dümenil et al. (1993), and including the Mississippi, Apalachicola and the Alabama rivers in the GOM.

In HYCOM, the model state consists of the following variables: baroclinic velocity components, barotropic velocity components, barotropic pressure, salinity, temperature and layer thickness (U, V, Ub, Vb, Pb, S, T and Thk). The diagnosed model SSH is the steric height anomaly that varies due to the barotropic pressure mode, the deviations in temperature and salinity and does not include the inverse barometer effect (atmospheric pressure) for consistence with the SLA measurements.

The SLA needs to be referred to a mean SSH. A 2-yr average of TOPAZ3 SSH is interpolated to our local grid (Fig. 1). It shows a maximum in LC, a positive track of SSH induced by the passage of eddies that drift westwards. It qualitatively compares well with the mean dynamic topography based on interpolated satellite and in situ measurements (Rio and Hernandez, 2004).

The probability density function (PDF) of the model state variables is assumed to be Gaussian in the EnOI. Thacker (2007) highlights that the Gaussian distribution is truncated in HYCOM for the layer thickness and for the sea surface temperature (SST)

when freezing/evaporation occurs, which can cause a problem for DA purpose. Here, a post-processing is applied to ensure that the layer thickness remains positive, and the issue of evaporation is addressed further in the study, but a more appropriate manner to deal with these problems is described in Thacker (2007).

3. Static ensemble multivariate covariances

In this study, the historical ensemble is composed of 122 weekly model outputs over a 2.5-yr period. To avoid spurious correlations, it is important to maintain the homogeneity in the sample. Therefore, the sample is gathered from a model already in equilibrium, with constant parameter setting and without DA. Section 2.1 pointed out that the efficiency of the EnOI is dependent on how well the ensemble of state represents the variability of the system, and on how linear the correlations are. To evaluate the realism of the correlations extracted from the static ensemble, we review them against our knowledge of the local dynamics. In particular, we analyse the correlation of SSH with the surrounding surface velocities and with the water column properties. Finally, we analyse the linearity of the dominant multivariate relationships using scatterplots. Statistical analyses of data points throughout the GOM reveal two typical locations, and these are presented here. The first location is in the central part of the GOM away from the shelf area, see Section 3.1. The second point is in a near coastal area, on the upper slope of the northern shelf, close to the Mississippi Delta, see Section 3.2.

3.1. Interior of the GOM

In the interior of the GOM, a positive anomaly in the SSH is representative of an anticyclonic circulation, that is, LC intrusion or anticyclonic eddies. These anticyclonic circulations are composed of YCW that differs from the resident GCW (Schmitz et al., 2005a). The ensemble correlations are analysed at a potential area of shedding (87.3°W, 26.3°N).

Figure 2 shows the horizontal correlation between SSH and the velocity field. The arrows correspond to the correlation between SSH and the total eastward (Ut) and northward (Vt) velocity component. The background colour highlights regions where the correlations with the eastward and northward velocities are large as

$$C = \sqrt{\text{corr(SSH, Ut)}^2 + \text{corr(SSH, Vt)}^2}. \tag{7}$$

An increase of the SSH at the target point is strongly positively correlated with a current ring that has a radius slightly smaller than 200 km. It agrees well with the average size of the eddies in the GOM, between 300 and 400 km (Vukovich, 2007). There is a slight anisotropy of the ring due to the interaction with the resident LC.

An increase of the SSH at the target point is also positively correlated with a dominant cyclonic circulation at its
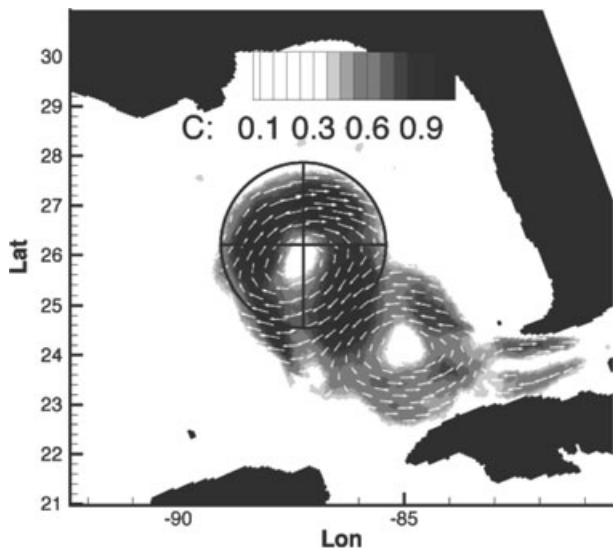
Fig. 2. Ensemble correlation plots between the SSH point marked by a cross and the surface currents in all model gridpoints in the Gulf of Mexico. The white arrows represent the correlation with total eastward and northward velocities. The background colour highlights regions where the correlations with the total eastward and northward velocities are large ($C > =0.35$, see eq. 7). The circle represents the area of localization (Section 3.3).

southeastern side, and in a minor way (approximately 0.30) with further cyclonic circulations along the perimeter of the main anticyclonic circulation. Depending on the location of the target point, the correlations indicate preferential locations of the cyclonic eddy around the main anticyclonic circulation anomaly. Theses cyclonic eddies in the GOM may play a key role in the shedding process (Schmitz et al., 2005b). However, a static ensemble approach may not be sufficient to deduce their positions from the location of the main anticyclonic eddy, because their behaviour and their growth are highly non-linear (Cherubin et al., 2005b). Therefore, it does not seem appropriate to let the assimilation act outside of the 200 km radius (black circle in Fig. 2).

Figure 3b shows the vertical correlation between SSH and the layer thickness profile at the target point. An increase of SSH implies a strong deepening of the upper layers of the model. In compensation for the deepening of the surface layers, the thickness of the layers located below 500 m is reducing.[1] These correlations are in good agreement with geostrophy, and with the vertical structure of an anticyclonic eddy in the GOM. The negative correlation found at 150 m is discussed below, following the correlation between SSH and temperature and salinity.

Figure 3a shows the correlation profile of temperature and salinity with SSH at the first target point. At the surface, the

---

[1] The layer depths are indicative since they correspond to their average over the ensemble. In general, the active layer of the LC extent is approximately 700 m deep and can reach 1000 m deep.
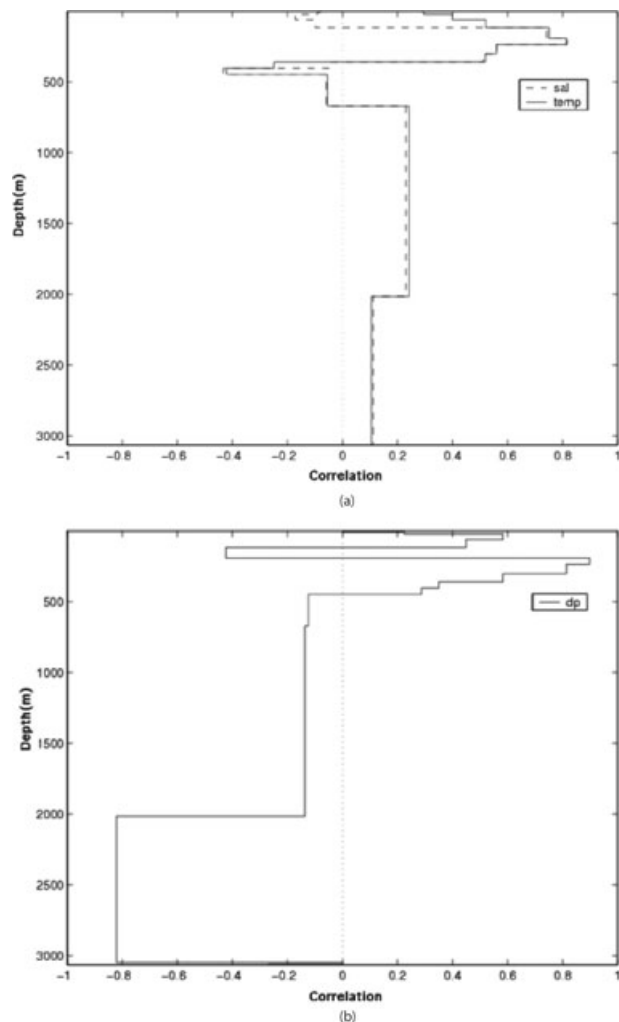

Fig. 3. (a) Correlation profile between SSH and temperature (solid line) and salinity (dashed line) at a target point located in the central GOM; (b) correlation profile of the layer thickness with SSH at the same target point. The depths of the layers are the average over the ensemble.

SSH is positively correlated with temperature and slightly negatively correlated with salinity. The YCW is warmer at the surface because it is advected from tropical regions, and fresher near surface due to the influence of the Amazon and the local dilution in the Caribbean Sea (Rivas, 2005). The linearity of the correlation between SSH and near surface temperature (30 m) is represented in the scatterplot (Fig. 4a). Below 27°C, the correlation between SSH and temperature is positive and arguably linear, whereas above 27°C, no correlation is evident. Hence, a uniformly warm mixed layer develops over the top 150 m during the summer months in the GOM, and the temperature saturates. This example shows one limitation of the multi-Gaussian hypothesis.

The correlations of SSH with temperature and salinity reach a maximum for both variables between 150 and 200 m. Such
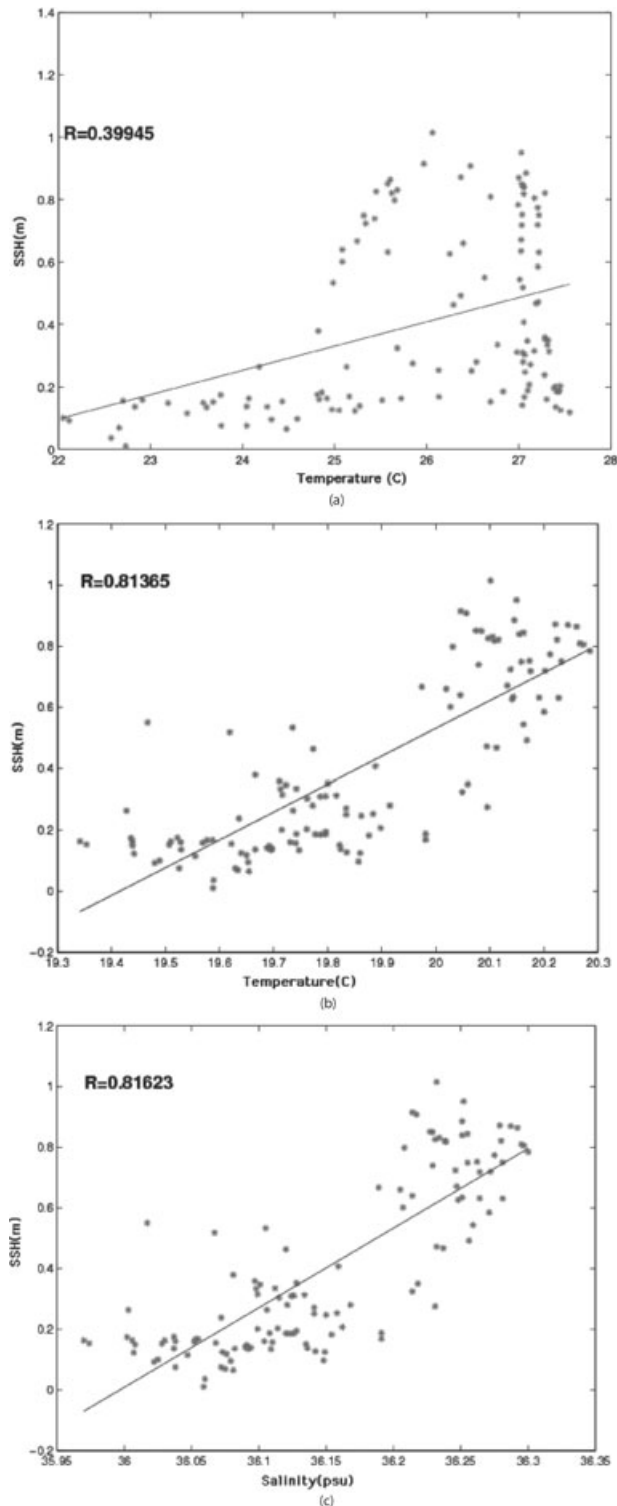
depths correspond to the warm and saline SUW core found at intermediate depths in the YCW that composes the eddy. The linearity of these correlations is analysed by using scatterplots of temperature and salinity with SSH (see Figs. 4b and c). Two groups of points that correspond to the different water masses (SUW and GCW) can be recognized. Although a bimodal representation of the correlation might be more appropriate, a linear approach remains satisfactory in this case, because the distance between the two groups is smaller than the variability within each group. The negative correlation found at about 150 m between SSH and layer thickness can be explained by comparing Figs. 3a and b. It corresponds to the layer above the SUW layer. In the EnOI, an increase of SSH stretches the core of SUW at the expense of the above layer thickness as previously suggested by the measurements (fig. 1 in Elliott, 1982).

The correlations are then negative around 500 m for salinity and temperature, induced by the presence of the fresher water in the YCW.

At depth, the correlations are below 0.2, and can be considered insignificant with respect to those discussed above. This seems realistic, since the main differences between the YCW and the GCW occur within the upper 700 m.

This vertical correlation shows an advantage of the EnOI over the methods that are not entirely multivariate (e.g. Cooper and Haines, 1996), because the impact on temperature and salinity are representative of the local eddy stratification. However, the multivariate correlation might not be valid for correcting the position of an eddy in water that has uniform properties (e.g. cyclonic eddies). In which case, a dynamic ensemble may be more appropriate. We expect the latter situation to be marginal by comparison to the positioning of the LC and its anticyclonic eddies.

3.2. Upper slope

The dynamics on the upper slope are influenced by the coastal dynamics. In particular at the studied location where the Mississippi and the neighbouring Atchafalaya rivers contribute approximately 2/3 of the 30 000 $m^{-3}\,s^{-1}$ fresh water released into the GOM (Morey et al., 2003). DA near coastal areas is a real challenge, since the circulation is usually complex and measurements are less accurate. The correlations are analysed at a point located on the upper slope of the northern shelf close to the Mississippi Delta (88.6°W, 28.7°N) in water sufficiently deep (approximately 1000 m) so that data can be assimilated. The variability of the SSH and thus the EnOI representation of the forecast error variance is much smaller in coastal areas than in the centre of the basin. It implies that the impact of assimilation will be less than in deep waters.

The horizontal correlation between SSH and SST (larger than 0.8; see Fig. 5) is stronger than the one between SSH and the surface velocity (smaller than 0.5 in Fig. 6). This correlation is clearly linear (see Fig. 5) and can be explained by thermal

Fig. 4. Scatterplots of SSH versus temperature near surface (a); at layer 8 (1025.68 kg m^{-3} reference density, $\simeq$200 m) (b) and versus salinity at layer 8 (c), at the first target point. The thick line denotes the linear regression, and *R* denotes the coefficient of correlation.
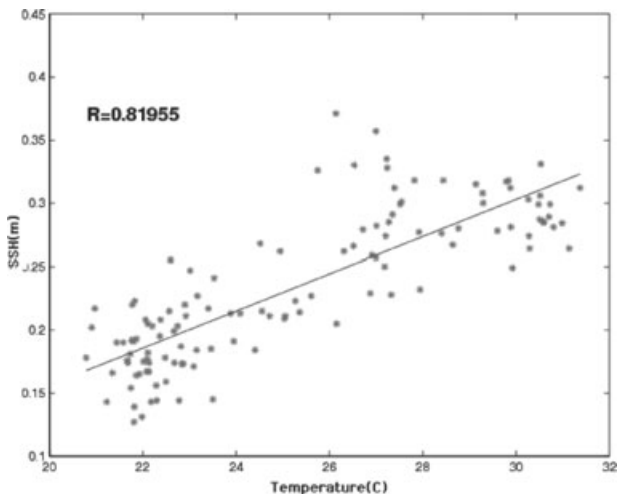
Fig. 5. (a) Correlation profile between SSH and temperature (solid line) and salinity (dashed line) at a target point located close to the northern shelf; (b) correlation profile of the layer thickness with SSH at the same target point. The depths of the layers are the average over the ensemble.
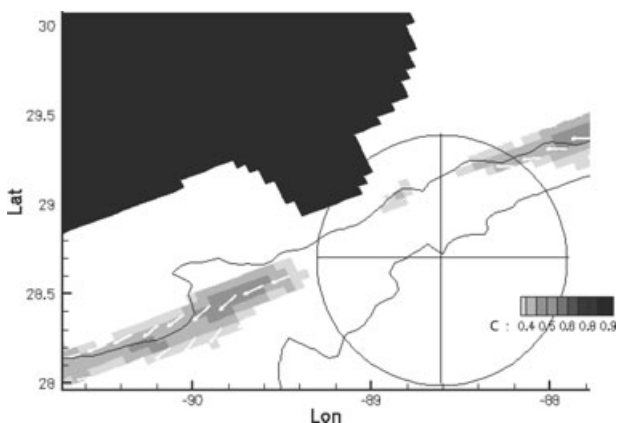

Fig. 6. Scatterplot of SST versus SSH at the target point. The thick line denotes the linear regression, and R denotes the coefficient of correlation between the two variables.
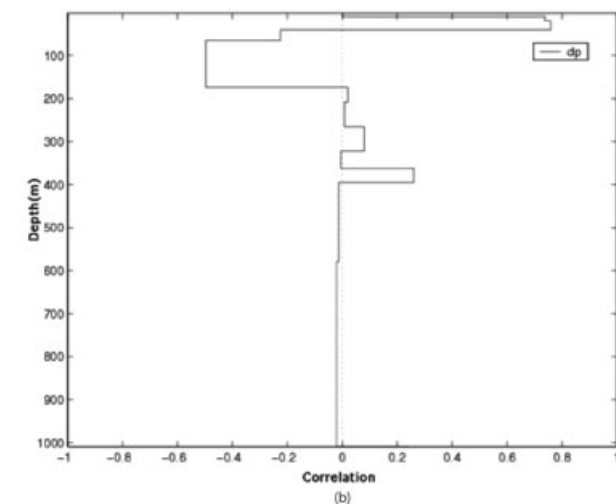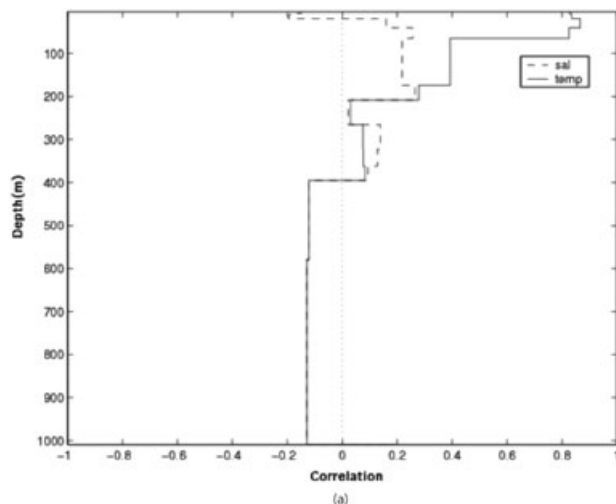
Fig. 7. Ensemble correlation plots between the SSH point marked by a cross and the surface currents in the northern shelf of the GOM. The white arrows represent the correlation with eastward and northward velocities. The background color highlights regions where the correlations with the total eastward and northward velocities are large ($C > =0.35$, see eq. 7). The black lines represent the 100 and 1000 m isolines. The circle represents the area of localization (Section 3.3).

expansion. Therefore, at the target point, the variability of SSH is mainly controlled by seasonal variability. There is also weak correlation with small vortices, but it is largely dominated by the seasonal signal.

Figure 6 represents the correlation between SSH and the surface velocity at the second target point, in a similar way as for the first target point. Although the correlations are much weaker, a high SSH is positively correlated with a westward shelf current. This contradicts the results from Morey et al. (2003), where the winds enhance a westward coastal shelf current during winter time and an eastward coastal shelf current during the summer months, in the northern shelf. However, our point is located further away (on the upper slope) from the coastal area described in Morey et al. (2003), which could explain some of the dis-

crepancies. In our ensemble run, the residual shelf correlation is induced by the interaction of small vortices[2] with the shelf, as described in Hamilton and Lee (2005). This mechanism is more frequently observed during summer than during winter in our historical run. A longer ensemble run should average out this artificial correlation, and the expected correlation induced by winds might then prevail.

In Figs. 7a and b, the vertical correlation is restrained to the upper 200 m. The correlation between SSH and the layer thickness is positive in the top 30 m and then reverses between 30 and 200 m. The vertical correlation of temperature with SSH

[2] with a radius smaller than 75 km.

(Fig. 7a) is uniformly positive in the top 50 m and decreases slowly until 200 m. An SSH increase is positively correlated with an increase of the salinity gradient, that is, fresher at the surface and more saline below the first 20 m. These correlations reflect the seasonal stratification differences between summer (high SSH) and winter, in good agreement with the climatology.

3.3. Localization

The range of significance of a measurement is a critical question in assimilation. In the present case, it is unrealistic that a measurement in the western GOM contributes towards resolving the circulation in the eastern basin. In Fig. 2, an increase of SSH in the middle of the basin is positively correlated with an anticylonic circulation on the western side of the GOM, and with an intensification of the Florida current. This is likely a spurious long-range correlation due to the limited sample of members, and we should therefore limit the horizontal extent of the updates.

To implement the localization Evensen (2003) suggests a multiplication of the innovations (denoted by $\mathbf{d} - \mathbf{H}\boldsymbol{\psi}^{\mathrm{f}}$ in eq. 5), by a step function. We ensure instead a smooth transition at the edges of the localization area by applying weight function (W) to the innovations, which depends on the distance between the observation points (x), on the target model point (x_0) and on the localization radius (r_0).

$$W = \begin{cases} 1 & : \text{if } |x - x_0| < \frac{r_0}{2} \\ \frac{1}{2}\left(1 + \cos\left(\frac{2\pi(|x-x_0| - \frac{r_0}{2})}{r_0}\right)\right) & : \text{if } \frac{r_0}{2} < |x - x_0| < r_0 \quad (8) \\ 0 & : \text{otherwise.} \end{cases}$$

Oke et al. (2005) use a localization method that acts on the covariance matrix rather than on the innovations. They apply localization by a Schur product on the error covariance matrix ($\mathbf{A}' \, \mathbf{A}'^{\mathrm{T}}$) with a quasi-Gaussian function.

A drawback of the localization is that it can breakdown the conservation of the geostrophic balance. Oke et al. (2007) show that localization conserves the geostrophic balance, when the radius of the localization is equal to, or larger than the radius of decorrelation (i.e. where the correlations become insignificant).

The scales of the features present in the SSH are small compared to the size of the GOM. We observe that the correlations become smaller in scale when the target point is chosen closer to the coast. Therefore, the localization radius is set dependently on the water depth, such that it linearly reduces from 200 km in the deep GOM to 25 km at the limit of the assimilation domain (300 m deep). In the central GOM, the dominant decorrelation radius has the size of anticyclonic eddies ($\simeq$200 km). Hence in Fig. 2, a decorrelation radius of 200 km (black circle) seems appropriate. It contains the geostrophic ring but does not include the correlation with the surrounding cyclonic eddies. In the second target point, the correlations are dominated by seasonal variability. To forecast the position of eddies, one would

prefer to correct the mesoscale eddies of diameter less than 150 km (Hamilton and Lee, 2005), which can interact with the large eddy shed from the LC on the northern shelf. Therefore, a 75 km radius contains the dominant state variable correlations (temperature, SSH), and cuts off the artificial correlation with the shelf current. The EnOI will thus act like a simple OI on the horizontal direction, and with the use of interpolated maps, will be able to represent the mesoscale eddies. The multivariate impact on velocity will be very small as correlations are almost null within the circle. But luckily, the seasonal variability and the passage of anticyclonic eddies have a relatively similar impact on the water column, (see plate 3 in Hamilton and Lee, 2005), and the correlation with the stratification will be well suited. However, we would like to emphasize that the approach used here is theoretically not satisfactory, and that a more appropriate approach could be achieved by removing the seasonal variability (Sakov and Oke, 2005).

4. Assimilation updates

In Section 3, the ensemble covariance is found in agreements with the known circulation in two characteristic locations. But in practical use, satellite altimeter measurements are numerous and spread all over the domain. The accuracy of the DA system is demonstrated for the 5 July 2006 prior to the shedding of Eddy Yankee, which is observed from altimeters around the 19 July 2006.

A shedding event involves the rapid growth of non-linear instabilities that are difficult to forecast (Cherubin et al., 2005b). In particular, Eddy Yankee has been problematic for the offshore oil and gas industry operating in the northern shelf of the GOM.

The initial state has undergone 1 month of weekly assimilation cycles prior to the period of study, to bring the model relatively close to reality and to emulate an operational setting. A value of $\alpha = 0.09$ is found to be optimal as it combines efficient updates and stability. This value is therefore used in the experiments below.

The multivariate consistency of the assimilation is analysed in Section 4.1. The accuracy of the model forecast following the assimilation is analysed in Section 4.2.

4.1. Multivariate consistency

Figure 8a shows the model SSH and currents before assimilation, Fig. 8b after assimilation, and Fig. 8c corresponds to the SSH measurements that are assimilated into the model.

Before assimilation, the model LC has a similar penetration as described in the measurements, and cyclonic eddies can be found on either side of the LC neck, which indicates a near-shedding situation. However, the shedding event has advanced further in the measurements, with a distinct eastern cyclonic eddy that penetrates deeper into the LC. The shape of the northern tip of the LC is too circular in the model, and does not have the same
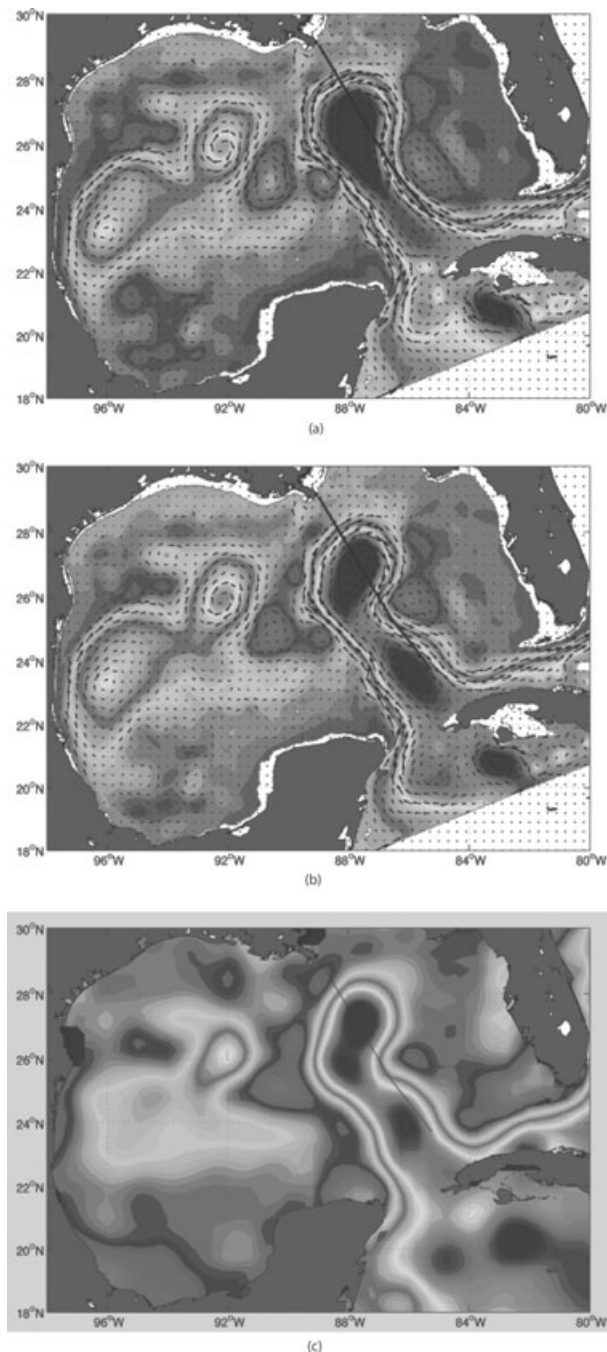
Fig. 8. (a) SSH Model Forecast for the 5 July 2006; (b) analysed state for the same date (c) Ssalto/Duacs altimetry measurement provided by CLS used for assimilation. The thick black line corresponds to the section analysed in Fig. 9.

'peanut' shape as in the measurements. The cyclonic eddy to the north is also too weak in the model.

The assimilation has corrected most of the discrepancies between the model and the observed SSH, and the resulting currents are in good agreement with the geostrophy. The vertical projection of the assimilation is analysed across a section that

shows the strongest SSH increments (marked by a black line on Fig. 8a).

The multivariate updates are presented in Fig. 9, with vertical section plots of, temperature and salinity before assimilation, SSH increments, and the corresponding temperature and salinity increments with the layer interface of the analysed state. The increments within each isopycnal layer are small, and rarely exceed $1°$ in temperature and 0.1 psu in salinity. The impact on temperature and salinity corresponds relatively well to the correlation found earlier in Section 3. Namely, there is a freshening of surface salinity, an increase of the intermediate layer salinity, an increase of the near surface and intermediate temperature and a deepening of the top layers. The changes do not always occur in the same layer, and as they approach the northern shelf, the updates are closer to the surface.

4.2. Forecasting skills

To assess the skill of the model forecast, the forecast errors are compared against posterior SSH data, with respect to the skill of a trivial predictor (persistence) and those of the model without assimilation. The rms error of model SSH against SLA track data is computed after the assimilation for the model without assimilation, for the persistence (of the analysed state), and for the model forecast following the assimilation. During a shedding event, the fast dynamics of the eastern GOM contrast with the slower activity of the remaining domain, and the rms errors vary from day-to-day, due to irregular sampling of satellite tracks. Over 3 d, the track data cover the domain relatively uniformly, and in Fig. 10, the rms errors are averaged over 3 d and over the whole domain except for the first and last days of the study period.

The states that have undergone DA (i.e. the persistence and the forecast) are closer to observations than the non-assimilated state. It demonstrates the benefit of DA on the accuracy of the result, as expected. Although the difference is small at the beginning, the model forecast rms error is lower than the persistence. It shows that the model provides an added value compared to the analysis. One may expect a quick increase of the rms errors in case of violent adjustments after assimilation, but here, the forecast beats the persistence from the first day after assimilation. The relatively slow increase of the rms error indicates that the accuracy of the prediction up to two weeks, is more dependent on the accuracy of the initial state than on the skill of the dynamical model, consistently with Oey et al. (2005a).

4.3. Generation of gravity waves

A general concern about DA is the possible generation of spurious gravity waves, when the method does not maintain the model balance (i.e. equilibrium of the pressure field). Theses waves may propagate into the model and interfere with its dynamics. With the EnOI, the updates are a combination of model
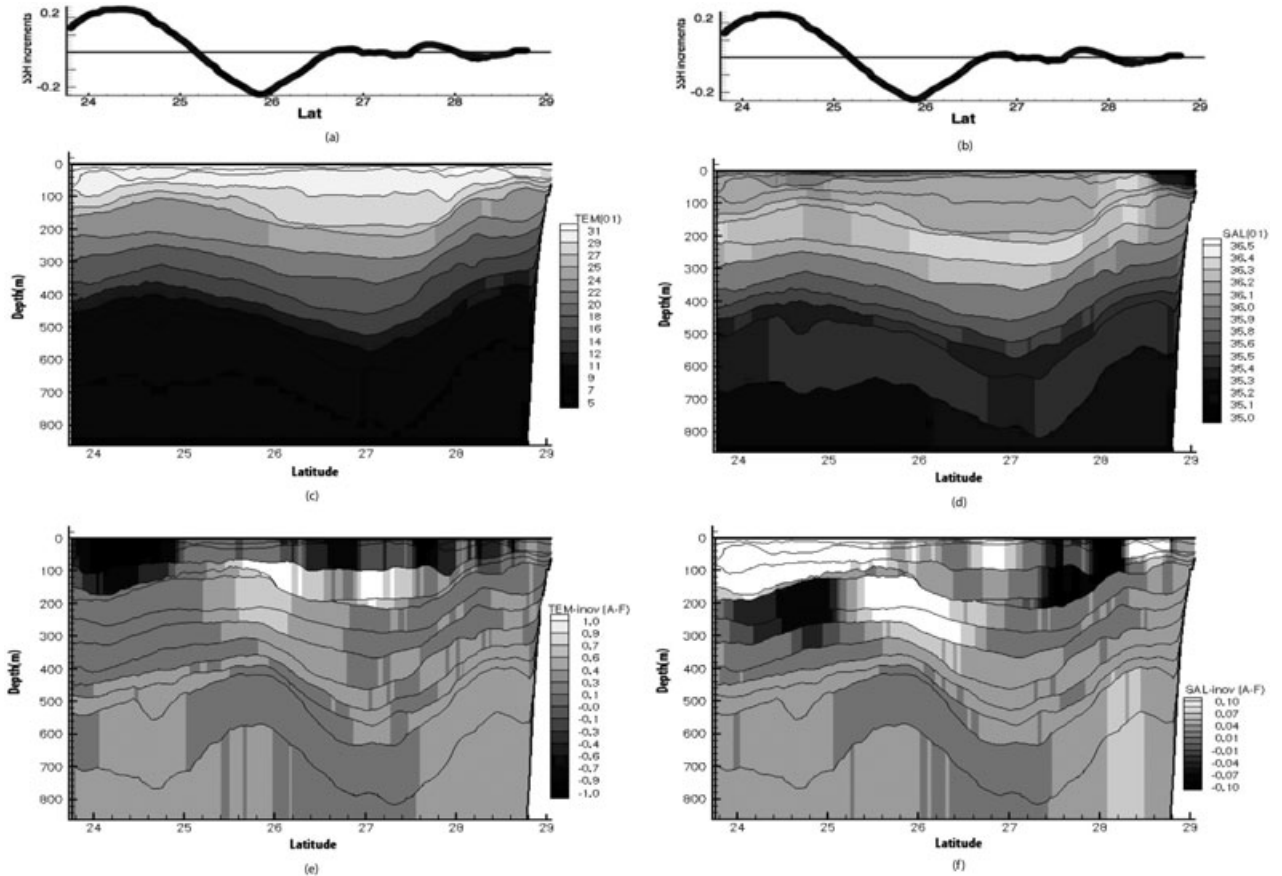
Fig. 9. SSH increments along the section (a and b). Vertical section plot before assimilation of temperature (c) and salinity (d). Analysed state layer interface with increments of temperature (e) and salinity (f).
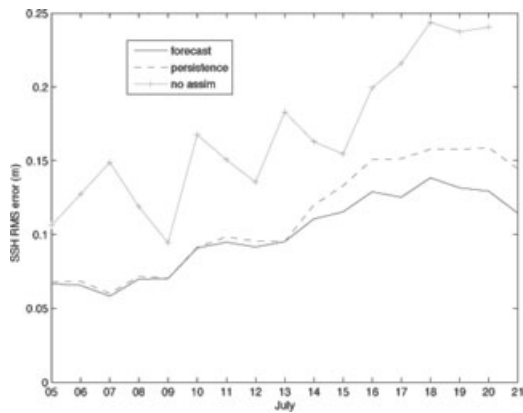

Fig. 10. Daily rms error of the model against SSH track data (3 d centered average). The solid line corresponds to the model forecast after assimilation, the dashed line to the persistence and the cross-solid line to the model run without assimilation.

states, which implies that the model balance is conserved as long as the model is linear. However Oke et al. (2007) show that an inappropriate localization radius can compromise the model balance and artificially amplify the high-frequency waves.

The computation of density from temperature and salinity is non-linear in HYCOM. The combination of two isopycnal layer properties by a DA step generates a new water mass with a slightly different density due to caballing, which can alter the model stratification. We first analysed the overall stability of our EnOI set-up, and then quantify the contribution from the artificial caballing.

To enhance the spurious effects of assimilation, the DA exercise done previously in 4.1 (noted EnOI$_{\alpha=0.09}$) is reprocessed with an exaggerated large value of α (0.56 instead of 0.09, noted EnOI$_{\alpha=0.56}$) that will pull the model closer to observations by artificially reducing the observation error. The impact on the layer interface is studied along the section marked by a black line in Fig. 8a. This analysis focuses on the top 1000 m since the updates are smaller below. In Fig. 11, the background and the black lines correspond to the temperature section of the assimilated state, and the white lines correspond to the layer interface 6 h after assimilation. We expect the assimilation shock to displace the layer interfaces quickly during the 6 h that follow the assimilation by the creation of gravity waves. But, this is not the case indicating that even with an exaggerated value of α, only little noise is introduced. Some differences can be identified within the mixed
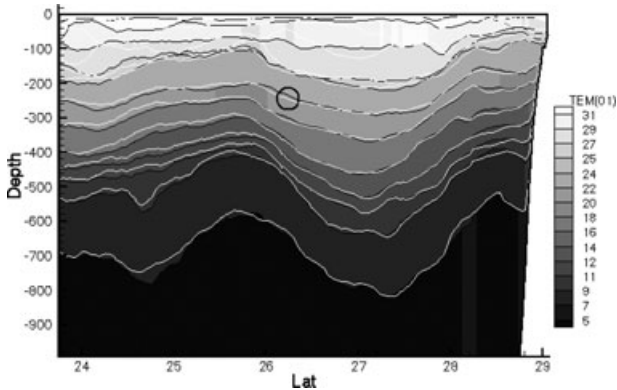
Fig. 11. Temperature section plot where the black lines correspond to the layer interface after assimilation with $\alpha = 0.56$, and the white lines correspond to the layer interface after 6 h of model run.

layer (approximately the top 100 m), but it has little effect on the model stability because the density changes are small and the mixing scheme damps them rather quickly. Smaller discrepancies can also be identified in the isopycnal layers, but it is hard to differentiate between normal model variability and readjustment caused by the assimilation. To clarify this issue, a time-series of an isopycnal layer depth is analysed by wavelet analysis at a point along the section where the assimilation updates were strong for layer thickness, temperature and salinity (at $26.2°$ N marked by a black circle on Fig. 11).

With the EnOI$_{\alpha=0.56}$ (Fig. 12b), one can observe a significant high-frequency noise (with a period lower than 4 h) not present on the run without assimilation (Fig. 12a). However, the model damps this artificial noise in less than 2 d. To determine whether the noise is originating from artificial caballing or from other sources (e.g. localization), an additional assimilation experiment (called EnOI-TS$_{\alpha=0.56}$) is performed with α set to 0.56, but with no change in temperature and salinity (i.e. only layer thickness and currents are updated). The initial high-frequency noise is no longer obvious, see Fig. 12c. Table 1 gives the variance of the high frequency (smaller than 4 h) of the different experiments.

The variance of the high frequency is reduced when neither temperature nor salinity is changed during assimilation, and the high frequency is almost reduced by half when the value of α is set to a more realistic level (EnOI$_{\alpha=0.09}$ experiment). The rest of the variance can be potentially explained by the localization method, as described in Oke et al. (2005).

5. Discussion and conclusion

This study analyses in some detail the EnOI, a computer efficient three-dimensional multivariate DA method, for assimilation of altimetry data in the GOM. The method relates the updates to different physical processes, depending on their geographical location. A careful analysis is carried out focusing on the reality of the correlation, regarding the known circulation of the area, and the linearity of these correlations, as assumed in the EnOI.
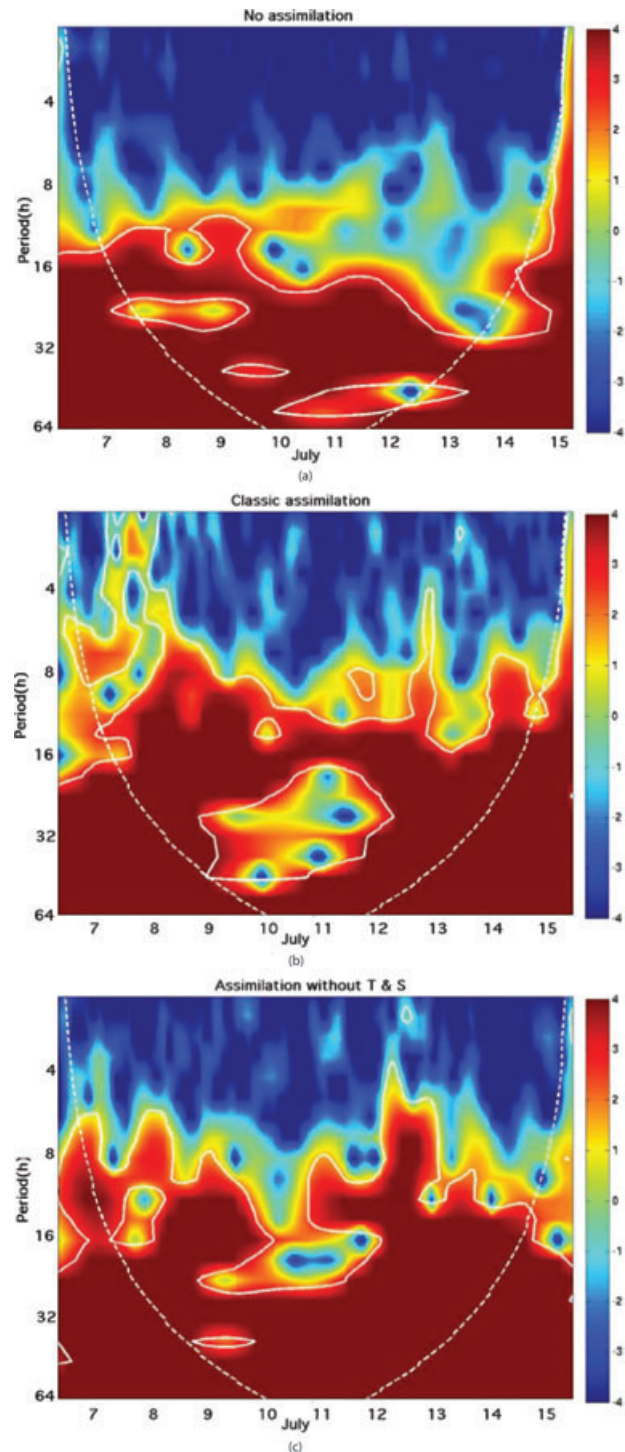

Fig. 12. Wavelet analysis of the layer 8 depth time-series in the control run (a), in EnOI$_{\alpha=0.56}$ (b) in EnOI-TS$_{\alpha=0.56}$ (c). The period unit is hours. The dashed white line corresponds to the boundary of the time interval, and the thick white line delimits the 95% significant confidence indices. The background is the log of the energy (m^2).

Table 1. Variance in m^2 of the high frequency (smaller than 4 h) for the first 5 d after assimilation

	Control	EnOI$_{\alpha=0.09}$	EnOI$_{\alpha=0.56}$	EnOI-TS$_{\alpha=0.56}$
α	0	0.09	0.56	0.56
Variable updated	None	All	All	No T&S
HF variance	1	2	3.9	2.6

This analysis is done at two characteristic locations that are related to different processes, in the central GOM and in the upper slope.

In the central GOM, a positive anomaly of SSH is related to the presence of an anticyclonic circulation. The correlations extracted from our historical ensemble are in good agreement with the properties of eddies in the GOM, their currents as well as their stratification, similarly to other methods such as Cooper and Haines (1996). In addition to that, the ensemble shows a correlation profile of temperature and salinity in good agreement with the water masses of eddies in the GOM.

In an upper slope area (northern shelf), the static ensemble correlations are dominated by seasonal variability. The correlations of SSH with temperature and salinity are in good agreement with the climatology, but a weak artificial correlation is found between SSH and the shelf current. This correlation is expected to disappear using a longer historical ensemble.

The assumptions of linear correlation made in the EnOI are approximately valid in the GOM. However, the scatterplots show some non-linearity. First, there is a saturation of the near surface temperature that will lead to an overestimate of the high temperature values (Fig. 4a). Second, there are different groups of members for the intermediate waters (Figs. 4b and c) in the centre of the basin. Mixing between these will lead to the formation of new water masses with intermediate water properties, which are not necessarily physical.

The saturation problem can be overcome by different solutions:

(1) Application of a simple post-processing that limits the maximum value obtained after assimilation to the range of the ensemble. This 'engineering fix' allows for a better representation of the variable but a multivariate fix of temperature and salinity would better preserve the model balance.

(2) Using different ensembles, that is, one with the variable saturation and the other one without. Concerning the SST example, the 'non-summer' ensemble will potentially present higher correlation between SST and SSH, whereas the 'summer' might not show any. This is one of the advantages of the EnKF over the EnOI, since all the members are realizations of the model at the time of assimilation, and that the risk of including alternate mechanisms (e.g. seasonal) is reduced.

Concerning the different groups of populations found in Figs. 4b and c, a bimodal representation of the relationship might be more appropriate. However, such problems are difficult to handle in practice and a linear approach so far seems satisfactory. Note that the classical EnKF is also unsuited to bimodal distributions.

If one intends to forecast the eddy shedding in the GOM, the DA method should correct the position of the main eddies in the centre of the basin and the small-scale eddies in the upper shelves area. In this concern, the EnOI appears to be suitable for the centre of the basin, but not in the upper-shelf area, as seasonal variability dominates there. To limit this impact, we suggest to use a variable localization radius that increases with depths, such that the radius is equal to the size of the vortices. Although this fix seems relatively efficient, one should consider removing the seasonal cycle from the ensemble, or using a dynamical ensemble.

Although the dynamical balance is relatively well respected with the EnOI, high-frequency oscillations (period smaller than 4 h) are introduced at the layer interface, partially caused by artificial caballing during assimilation. One counter-measure would be to update only temperature (or salinity) in the isopycnal layers and then diagnose salinity (or temperature) from the equation of state, as it is done for the MVOI (Cummings, 2005). One should then identify which is the controlling variable, temperature or salinity. This may lead to a practical problem because the controlling variable might change depending on the geographical location. Furthermore, the diagnosed variable might be less accurate than the one obtained by assimilation. Therefore, a more appropriate approach could be to apply the anamorphosis method described in Bertino et al. (2003). A non-linear transformation of temperature and salinity could then be devised such that the transformed variables are linearly related to density. This would ensure that the assimilation applied to the transformed variables does not induce artificial caballing.

Finally, the EnOI succeeds in terms of forecasting skill compared to the non-assimilated state and the trivial predictor (i.e. persistence). Additionally, the example confirms the importance of an accurate initial state over a good dynamical model for forecasts up to 14 d long.

6. Acknowledgments

References

Abascal, A., Sheinbaum, J., Candela, J., Ochoa, J. and Badan, A. 2003. Analysis of flow variability in the Yucatan Channel. *J. Geophys. Res.* **108**, 3381–3399.

Bennett, A. F. 2002. *Inverse Modeling of the Ocean and Atmosphere*. Cambridge University Press, New York, 234 pp.

Bentsen, M., Evensen, G., Drange, H. and Jenkins, A. D. 1998. Coordinate transformation on a sphere using a conformal mapping. *Mon. Wea. Rev.* **127**, 2733–2740.

Bertino, L., Evensen, G. and Wackernagel, H. 2003. Sequential data assimilation techniques in oceanography. *Int. Stat. Rev.* **71**, 223–242.

Bleck, R. 2002. An oceanic general circulation model framed in hybrid isopycnic-Cartesian coordinates. *Ocean Model.* **4**, 55–88.

Brasseur, P. and Verron, J. 2006. The SEEK filter method for data assimilation in oceanography: a synthesis. *Ocean Dyn.* **56**, 650–661.

Browning, G. L. and Kreiss, H.-O. 1982. Initialization of the shallow water equations with open boundaries by the bounded derivative method. *Tellus* **34**, 334–351.

Chassignet, E. P., Hulburt, H. E., Smedstad, O. M., Barron, C. N., Ko, D. S., and co-authors. 2005. Assessment of data assimilative ocean models in the Gulf of Mexico using ocean color. In: *Circulation in the Gulf of Mexico: Observations and Models* Volume 161. American Geophysical Union, 87–100.

Cherubin, L. M., Morel, Y. and Chassignet, E. P. 2005b. The role of cyclones and topography in the Loop Current ring shedding. *J. Phys. Oceanogr.* **31**, 569–591.

Cooper, M. and Haines, K. 1996. Altimetric assimilation with water property conservation. *J. Geophys. Res.* **101**, 1059–1077.

Cummings, J. 2005. Operational multivariate ocean data assimilation. *R. Meteorol. Soc.* **131**, 3583–3604.

Dai, A. and Trenberth, K. 2002. Estimates of freshwater discharge from continents: land seasonal variations. *J. Hydrometeorol.* **3**, 660–687.

Ducet, N., Le Traon, P. and Reverdin, G. 2000. Global high-resolution mapping of ocean circulation from TOPEX/Poseidon and ERS-1 and-2. *J. Geophys. Res.-Oceans* **105**, 19 477–19 498.

Dümenil, L., Isele, K., Liebscher, H., Schröder, U., Schumacher, M. and co-authors. 1993. *Discharge Data from 50 Selected Rivers for GCM Validation*, Max-Planck-Institut für Meteorologie.

Evensen, G. 2003. The Ensemble Kalman Filter: theoretical formulation and practical implementation. *Ocean Dyn.* **53**, 343–367.

Evensen, G. 2006. *Data Assimilation: The Ensemble Kalman Filter*, Springer-Verlag New York, Inc. Secaucus, NJ, USA.

Elliott, B. A. 1982. Anticyclonic rings in the Gulf of Mexico. *J. Phys. Oceanogr.* **12**, 1291–1309.

Fox, D., Teague, W., Barron, C., Carnes, M. and Lee, C. 2002. The Modular Ocean Data Assimilation System (MODAS). *J. Atmosp. Ocean. Technol.* **19**, 240–252.

Hamilton, P. and Lee, T. 2005. Eddies and jets over the slope of the northeast Gulf of Mexico. *Geophys. Monogr.* **161**, 123–142.

Kalman, R. 1960. A new approach to linear filtering and prediction problems. *J. Basic Eng.* **82**, 35–45.

Kantha, L., Choi, J. K., Schaudt, K. J. and Cooper, C. K. 2005b. A regional data-assimilative model for operational use in the Gulf of Mexico. Circulation in the Gulf of Mexico: observations and models. *Am. J. Atmos. Ocean. Technol.* **25**, 794–806.

Le Traon, P. Y., Dibarboure, G. and Dorandeu, J. 2003. SSALTO/DUACS and operational altimetry. In: *Geoscience and Remote Sensing Symposium. IGARSS'03. Proceedings. 2003 IEEE International*.

Morey, S. L., Martin, P. J., O'Brien, J. J., Wallcraft, A. A. and Zavala-Hidalgo, J. 2003. Export pathways for river discharged fresh water in the northern Gulf of Mexico. *J. Geophys. Res.* **108**, 3303–3318.

Oey, L., Lee, H. and Schmitz, W. Jr., 2003. Effects of winds and Caribbean eddies on the frequency of Loop Current eddy shedding: a numerical model study. *J. Geophys. Res.* **108** (10.1029).

Oey, L., Ezer, T., Forristall, G., Cooper, C., DiMarco, S. and co-authors. 2005a. An exercise in forecasting loop current and eddy frontal positions in the Gulf of Mexico. *Geophys. Rese. Lett.* **32**, L12611.

Oey, L. T., Ezer, T. and Lee, H. C. 2005b. Loop Current, rings and related circulation in the Gulf of Mexico: a review of numerical models. In: *Circulation in the Gulf of Mexico: Observations and Models* Volume 161. American Geophysical Union, 31–56.

Oke, P. R., Allen, J. S., Miller, R. N., Egbert, G. D. and Kosro, P. M. 2002. Assimilation of surface velocity data into a primitive equation coastal ocean model. *J. Geophys. Res.* **107**, 3122–3147.

Oke, P., Schiller, A., Griffin, D. and Brassington, G. 2005. Ensemble data assimilation for an eddy-resolving ocean model of the Australian region. *QJR Meteorol. Soc.* **131**, 3301–3311.

Oke, P., Sakov, P. and Corney, S. 2007. Impacts of localisation in the EnKF and EnOI: experiments with a small model. *Ocean Dyn.* **57**, 32–45.

Rio, M.-H. and Hernandez, F. 2004. A mean dynamic topography computed over the world ocean from altimetry, in situ measurements, and a geoid model. *J. Geophys. Res.* **109**, 1–19.

Rivas, D. 2005. The ventilation of the deep Gulf of Mexico. *J. Phys. Oceanogr.* **35**, 1763–1781.

Sakov, P. and Oke, P. R. 2007. Objective array design: application to the tropical Indian Ocean. *Geophy. Monogr.* **161**, 123–142.

Schmitz, W. J. 2005. Cyclones and westward propagation in the shedding of anticyclonic rings from the Loop Current. In: *Circulation in the Gulf of Mexico: Observations and Models* Volume 161. American Geophysical Union, 241–261.

Schmitz, W. J., Biggs, D., Lugo-Fernandez, A., Oey, L.-Y. and Sturges, W. 2005. A synopsis of the circulation in the Gulf of Mexico and on its Continental margins. In: *Circulation in the Gulf of Mexico: Observations and Models* Volume 161. American Geophysical Union, 11–29.

Sheinbaum, J., Candela, J., Badan, A. and Ochoa, J. 2002. Flow structure and transport in the Yucatan Channel. *Geophys. Res. Lett.* **29**, 10.1–10.4.

Sturges, W. and Leben, R., 2000. Frequency of ring separations from the loop current in the Gulf of Mexico: a revisited estimate. *J. Phys. Oceanogr.* **30**, 1814–1819.

Teague, W., Carron, M. and Hogan, P., 1990. A comparision between the Generalized Digital Environmental Model and Levitus climatologies. *J. Geophys. Res.* **95**, 7167–7183.

Thacker, W. 2007. Data assimilation with inequality constraints. *Ocean Model.* **16**, 264–276.

Vukovich, F. 1988. Loop Current boundary variation. *J. Geophys. Res.* **93**, 585–15.

Vukovich, F. M. 2007. Climatology of ocean features in the Gulf of Mexico Using satellite remote sensing data. *Am. Meteorol. Soc.* **37**, 689–707.

Winther, N. G., Morel, Y. and Evensen, G. 2006. Efficiency of high order numerical schemes for momentum advection. *J. Marine Syst.* **67**, 31–46.